Rheology of cohesive granular materials across multiple dense-flow regimes

Yile Gu, Sebastian Chialvo, and Sankaran Sundaresan

Rheology of cohesive granular materials across multiple dense-flow regimes

Yile Gu, Sebastian Chialvo, and Sankaran Sundaresan
Chemical and Biological Engineering Department,
Princeton University, Princeton, New Jersey 08540, USA
(Dated: August 26, 2014)

We investigate the dense-flow rheology of cohesive granular materials through discrete element simulations of homogeneous, simple shear flows of frictional, cohesive, spherical particles. Dense shear flows of non-cohesive granular materials exhibit three regimes: quasistatic, inertial, and intermediate, which persist for cohesive materials as well. It is found that cohesion results in bifurcation of the inertial regime into two regimes: (a) a new rate-independent regime and (b) an inertial regime. Transition from rate-independent cohesive regime to inertial regime occurs when the kinetic energy supplied by shearing is sufficient to overcome the cohesive energy. Simulations reveal that inhomogeneous shear band forms in the vicinity of this transition, which is more pronounced at lower particle volume fractions. We propose a rheological model for cohesive systems that captures the simulation results across four regimes.

I. INTRODUCTION

Flows of dense granular materials occur in both natural and industrial processes and exhibit a variety of distinct rheological behaviors. For non-cohesive particles, three flow regimes have been identified – namely, the quasistatic, inertial, and intermediate regimes [1–4] – each of which manifests different scalings of the mean stresses with shear rate and volume fraction. Numerous constitutive stress models have been constructed with these scalings in mind [2, 3, 5–10]. However, many granular flows involve cohesive interparticle forces for which the above models do not account. These cohesive effects are the primary focus of the present study.

Cohesion can result from a variety of sources – including van der Waals forces [11, 12], electrostatic forces [13], capillary forces [14], and solid bridges [15] – and has a strong impact on granular rheology. For example, agglomeration of particles has been observed in simulations of cohesive granular materials in various flow geometries [16–21]. Annular shear flow experiments [22] and plane shear simulations [18, 20, 23] have shown that cohesion increases the shear stress ratio η, defined as the ratio of shear stress τ to pressure p. Both simulations and experiments have shown that the discharge flow rate from a hopper decreases with increasing cohesion [24]. Rotating-drum experiments reveal that cohesion increases avalanche size and leads to robust pattern formation on the surface [25–27]. Despite the number of such phenomenological studies, there is relatively little literature on constituting the rheological effects of cohesion. One notable work is that of Rognon et al. [20], which presents modifications to friction and dilatancy laws for non-cohesive particles to account for the effects of cohesion observed in 2-D simulations. The present study goes beyond these earlier studies by exposing how the regime map for non-cohesive materials [1–4] is altered by the introduction of cohesion and formulating explicit models for the mean stresses.

In this paper, we investigate the rheology of cohesive granular materials through discrete element method (DEM) simulations of homogeneous, simple shear flows of frictional and cohesive particles. Most of the simulations presented here are based on a linear (Hookean) spring-dashpot model [28] for particle-particle interaction and a commonly used model for van der Waals force between particles [29]. The quasistatic regime where the stress is proportional to spring stiffness (and independent of shear rate), the inertial regime where stress is proportional to square of shear rate (and independent of spring stiffness), and the intermediate regime where stress depends on both shear rate and spring stiffness – reported previously for non-cohesive particles [2] – persist even when cohesion is added. The presence of cohesion is found to introduce a new rate-independent regime where the stress depends on the strength of cohesion. These regimes persist when the Hookean contact model is replaced by a Hertzian contact model as well as when the van der Waals force model is replaced with an alternate cohesion model proposed by Rognon et al. [20], illustrating the robustness of these regimes. Finally, we also modify the blended stress model proposed by Chialvo et al. [2] for dense flows of non-cohesive particles to obtain an analogous model for dense flow of cohesive particles.

II. SIMULATION METHODS

The DEM simulations [28] were performed using the molecular dynamics package LAMMPS [30]. Particles interact via repulsive spring-dashpot contact forces and attractive cohesive forces. In the spring-dashpot model, the normal and tangential contact forces on a spherical particle i resulting from the contact of two spheres i and

j with same diameter d are

$$\boldsymbol{F}_{n_{ij}} = f(\frac{\delta_{ij}d}{4})[k_n\delta_{ij}\boldsymbol{n}_{ij} - \gamma_n m_{\text{eff}}\boldsymbol{v}_{n_{ij}}], \qquad (1)$$

$$\boldsymbol{F}_{t_{ij}} = f(\frac{\delta_{ij}d}{4})[-k_t\boldsymbol{u}_{t_{ij}} - \gamma_t m_{\text{eff}}\boldsymbol{v}_{t_{ij}}], \qquad (2)$$

where δ_{ij} is the overlap distance, k_n and k_t are spring elastic constants, γ_n and γ_t are viscous damping constants, $m_{\text{eff}} = m_i m_j/(m_i + m_j)$ is the effective mass of spheres with masses m_i and m_j, $\boldsymbol{v}_{n_{ij}}$ and $\boldsymbol{v}_{t_{ij}}$ are the normal and tangential components of relative particle velocity, and $\boldsymbol{u}_{t_{ij}}$ is the elastic shear displacement. For Hookean contact, $f(x) = 1$, while for Hertzian contact, $f(x) = \sqrt{x}$. The magnitude of tangential force is limited by a static yield criterion, $|\boldsymbol{F}_{t_{ij}}| \leq \mu|\boldsymbol{F}_{n_{ij}}|$, where μ is the particle friction coefficient. We set values of $k_t/k_n = 2/7$ [31] and $\gamma_t = 0$. For Hookean contact, for the default case, γ_n is chosen such that the restitution coefficient $e = \exp\left(-\gamma_n\pi/\sqrt{4k_n/m_{\text{eff}} - \gamma_n^2}\right) = 0.7$. For Hertzian contact, we employ the same value for $\gamma_n/\sqrt{k_n/m_{\text{eff}}}$, but now the restitution coefficient e depends on the collision velocities.

To account for cohesion, an attractive force $\boldsymbol{F}_{n_{ij}}^C$ is included so that the total normal force between the particles becomes $\boldsymbol{F}_{n_{ij}}^T = \boldsymbol{F}_{n_{ij}} + \boldsymbol{F}_{n_{ij}}^C$. For van der Waals force model, the cohesive force between a pair of particles whose surfaces separated by a distance s is written as [29]

$$\boldsymbol{F}_{n_{ij}}^C = -\frac{Ad^6}{6s^2(s+2d)^2(s+d)^3}, \qquad (3)$$

where A is the Hamaker constant. It is assumed that the force saturates at a minimum cutoff distance, $s_{\min} = \theta d$ [29]. Additionally, since the magnitude of the cohesive force decreases rapidly with separation distance, a maximum cutoff distance $s_{\max} = d/4$ [18] is used to accelerate the simulation process; for $s > s_{\max}$, cohesive force is neglected.

We also investigated the alternate model of Rognon et al. [20],

$$\boldsymbol{F}_{n_{ij}}^C = -\sqrt{4k_n N_A \delta_{ij}}, \qquad (4)$$

where N_A is specified as an input. Note that, in the static limit, where the relative particle velocity is zero, for Hookean contact, the total normal force between two particles is $k_n\delta_{ij} - \sqrt{4k_n N_A \delta_{ij}}$. Accordingly, $-N_A$ is the maximum attractive force between the two particles, experienced when $\delta_{ij} = N_A/k_n$ [20].

Differences between these two cohesion models are significant. The cohesive force in the van der Waals model (Eqn. (3)) is present before the particles collide and does not increase with overlap between particles. In Eqn. (4), the cohesive force is only present when particles are in contact and increases with extent of overlap. Nevertheless, it will be seen that both models lead to qualitatively similar results, differing in quantitative details only modestly.

In the DEM simulations, assemblies of about 2000 monodisperse particles of diameter d and density ρ_s are placed in a periodic box with fixed volume V. Through the Lees-Edwards boundary condition [32], particles are subjected to homogeneous steady simple shear at a shear rate $\dot{\gamma}$. The macroscopic stress tensor is calculated as

$$\boldsymbol{\sigma} = \frac{1}{V}\sum_i\left[\sum_{j\neq i}\frac{1}{2}\mathbf{r}_{ij}\mathbf{F}_{ij} + m_i(\mathbf{v}_i')(\mathbf{v}_i')\right], \qquad (5)$$

where $\mathbf{r}_{ij}$ is the normal vector pointing from the center of particle j to that of particle i, and $\mathbf{v}_i'$ is the fluctuating velocity of particle i relative to its mean streaming velocity. This stress tensor is further ensemble-averaged over many time steps. Ensemble-averaged pressure and shear stress can thus be obtained as $p = (\sigma_{xx} + \sigma_{yy} + \sigma_{zz})/3$ and $\tau = \sigma_{xz}$. The stresses and shear rate are made dimensionless through scaling with d, ρ_s, and elasticity $k = k_n$. Note that the dimensions of the spring constants and damping coefficients differ for Hookean and Hertzian contacts. Thus, for example, stress will be scaled using k/d and k in Hookean and Hertzian contacts, respectively. As gravity is not included in the simulations, a modified Bond number Bo^* is introduced, which compares the maximum net cohesive force experienced by a particle to a characteristic contact force. For Hookean contact with the van der Waals force model, $Bo^* = F_{\text{coh}}^{\max}/(kd) \approx A/(24k\theta^2 d^2)$, where $F_{\text{coh}}^{\max}$ denotes the maximum cohesive force. For Hertzian contact with the van der Waals force model, $Bo^* = F_{\text{coh}}^{\max}/(kd^2) \approx A/(24k\theta^2 d^3)$. Simulation results indicate that the results are insensitive to the particular value for θ $(1.0 \times 10^{-5} \leq \theta \leq 4.0 \times 10^{-5})$ for specified value of Bo^*. For the results presented in this paper, $\theta = 4 \times 10^{-5}$ is chosen [18]. Finally, for Hookean contact with the alternate cohesion model, $Bo^* = N_A/(kd)$.

III. FLOW REGIMES

We first consider Hookean contact and van der Waals cohesion. Simulations are performed for various shear rates, volume fractions, friction coefficients, and modified Bond numbers. Figure 1(a) plots the scaled pressure pd/k against the scaled shear rate $\hat{\dot{\gamma}} = \dot{\gamma}d/\sqrt{k/(\rho_s d)}$ for non-cohesive particles with $\mu = 0.1$. Three regimes are present [1–4]: quasistatic at low shear rates and high volume fractions, inertial at low shear rates and low volume fractions, and intermediate at high shear rates and all volume fractions. The quasistatic and inertial regimes are separated by a critical volume fraction ϕ_c which is a function of μ as summarized in Table I. When cohesive forces are included, however, it is found that this regime map is modified, as shown in Figures 1(b) and (c), where Bo^* is 5×10^{-6} and 5×10^{-5} respectively. Some aspects remain unchanged: all three non-cohesive regimes persist with no change in $\phi_c(\mu)$, and the quasistatic and intermediate pressure values show no appreciable changes. However, the inertial regime is now bifur-

cated into two regimes occurring at different scaled shear rates: at higher $\dot{\hat{\gamma}}$ the flow remains inertial (i.e. exhibiting Bagnold scaling), while at lower $\dot{\hat{\gamma}}$ the flow becomes rate-independent. We term this latter, new regime the *cohesive regime*. As Bo^* increases, this cohesive regime expands to encompass a larger domain of $\dot{\hat{\gamma}}$, as illustrated in Figures 1(b) and (c). Simulations were also performed for a highly inelastic system by lowering e from 0.7 (default case) to 0.02. It was found that all four regimes persist even for such a highly dissipative system, with no discernible change in the magnitude of the jamming volume fraction. (See Figure 2).

In Figures 1 and 2, we present the results only from simulations in which the velocity profile in the statistical steady state is found to be linear indicating homogeneous shear. There is a conspicuous absence of simulation results in Figures 1(b)(c) and 2(b) at the lower volume fractions and shear rates in the region representing transition from cohesive regime to inertial regime. In this region, the velocity profiles are found to be inhomogeneous (see Appendix A for further details). These cases are not included in the analysis of the homogeneously sheared state presented here.

The cohesive regime corresponds well to previous results [18] which report the existence of a rate-independent regime due to cohesion. Also, the cohesive-to-inertial regime transition is in accord with results from dynamic shear cell experiments on slightly cohesive powders [22]; the pressure in these experiments is roughly rate-independent at low shear rates but increases significantly at higher shear rates. Finally, the impact of cohesion on the scaling of pressure with respect to shear rate is consistent with previous 2-D, constant-pressure shear simulations of Rognon et al. [20]. They utilize $N_A/(pd)$ to characterize cohesion and find that, when $N_A/(pd)$ is large, the solid fraction no longer varies with inertial number (defined by them as $\dot{\gamma}\sqrt{m/p}$ for particle mass m) in their dilatancy law, which corresponds to the rate-independent behavior we observe for the pressure in the cohesive regime. The present paper details where this new rate-independent cohesive regime is located in parameter space with respect to the other three regimes and, for the first time, provides a comprehensive regime map for dense flows of cohesive granular materials capable of explaining all of the above behaviors.

Because previous works (e.g. [20, 33]) demonstrate the importance of microstructure on dense granular rheology, we aim to explain the cohesive-to-inertial regime transition in terms of changes in microstructure. To this end, we study the average coordination number Z, which is defined as the average number of contacts per particle in the system. Specifically, $Z = 2n_c/n$, where n_c is the total number of contacts (with particle overlap) and n is the total number of particles in the system. When $\phi > \phi_c$, cohesion has negligible impact on Z across all shear rates (i.e. quasistatic and intermediate regimes), as seen in Figure 3(a). For $\phi < \phi_c$, cohesion has a weak impact on Z at high shear rates (i.e. inertial and intermediate regimes), but substantially increases the value of Z in lower shear rate region (i.e. the cohesive regime), as seen in Figure 3(b). Thus, cohesion has an appreciable impact on Z only in the cohesive regime, which is consistent with the pressure data shown in Figure 1. To make this observation more transparent, we present in Figures 4(a) and 4(b) the variation of pressure with shear rate corresponding to conditions in Figures 3(a) and 3(b), respectively. It is clear that cohesion has only a weak impact (if any) on pressure (and, as presented later, shear stress) in quasistatic, inertial, and intermediate regimes. The emergence of rate-independent regime because of the cohesive force can be reasoned through the average coordination number characterizing the microstructure. When a dense assembly of non-cohesive particles is subjected to steady (and slow) shear, jamming occurs at a critical volume fraction, ϕ_c, which depends on the particle-particle coefficient of friction [33, 34] and there is a corresponding average coordination number Z_c. Under dynamic conditions [33], the stress tracks Z more closely than the particle volume fraction. Hence it is more accurate to characterize the regimes in terms of Z and shear rate, than in terms of volume fraction and shear rate. This distinction is more apparent when particles interact cohesively. For non-cohesive assemblies in slow, steady shear, Z falls below Z_c, when ϕ drops below ϕ_c. In contrast, for cohesive assemblies, Z can remain large even when ϕ is lowered below ϕ_c, and force chains persist, leading to rate-independent regime. (Compare Figures 3(b) and 4(b).)

Another behavior connected to the coordination number is the expansion of the cohesive regime with increasing Bo^*, as illustrated in Figure 3(b). The critical shear rate which sets the boundary between the cohesive and inertial regimes scales with $\sqrt{Bo^*}$, as demonstrated in Figure 3(c), where data are collapsed by scaling the dimensionless shear rate with $\sqrt{Bo^*}$. The $\sqrt{Bo^*}$ scaling can readily be rationalized: when cohesive energy ($\sim Bo^*$) is overcome by the kinetic energy supplied by the shearing ($\sim \dot{\hat{\gamma}}^2$), the system transitions from cohesive regime to inertial regime. This transition in dependence of Z on shear rate between the cohesive regime and inertial regime is consistent with previous findings [18, 19].

The variation of Z with shear rate is analyzed in more detail by decomposing the average coordination number plotted in Figures 3(a)(b) into two components: one in the extension quadrants (Z_{ext}) and one in the compression quadrants (Z_{com}), as shown in Figures 5(a)(b). As one would expect, the average coordination number in the compression quadrants is always higher than the counterpart in the extension quadrants [35]. At a packing fraction of 0.62 (which is larger than ϕ_c), Z_{com} and Z_{ext} are essentially the same for cohesive and non-cohesive systems, see Figure 5(a). Furthermore, both of them remain nearly independent of shear rate at low shear rates, and decrease at higher shear rates; thus, there is no discernible difference in the behavior in the different quadrants. At packing fractions lower than ϕ_c, inertial
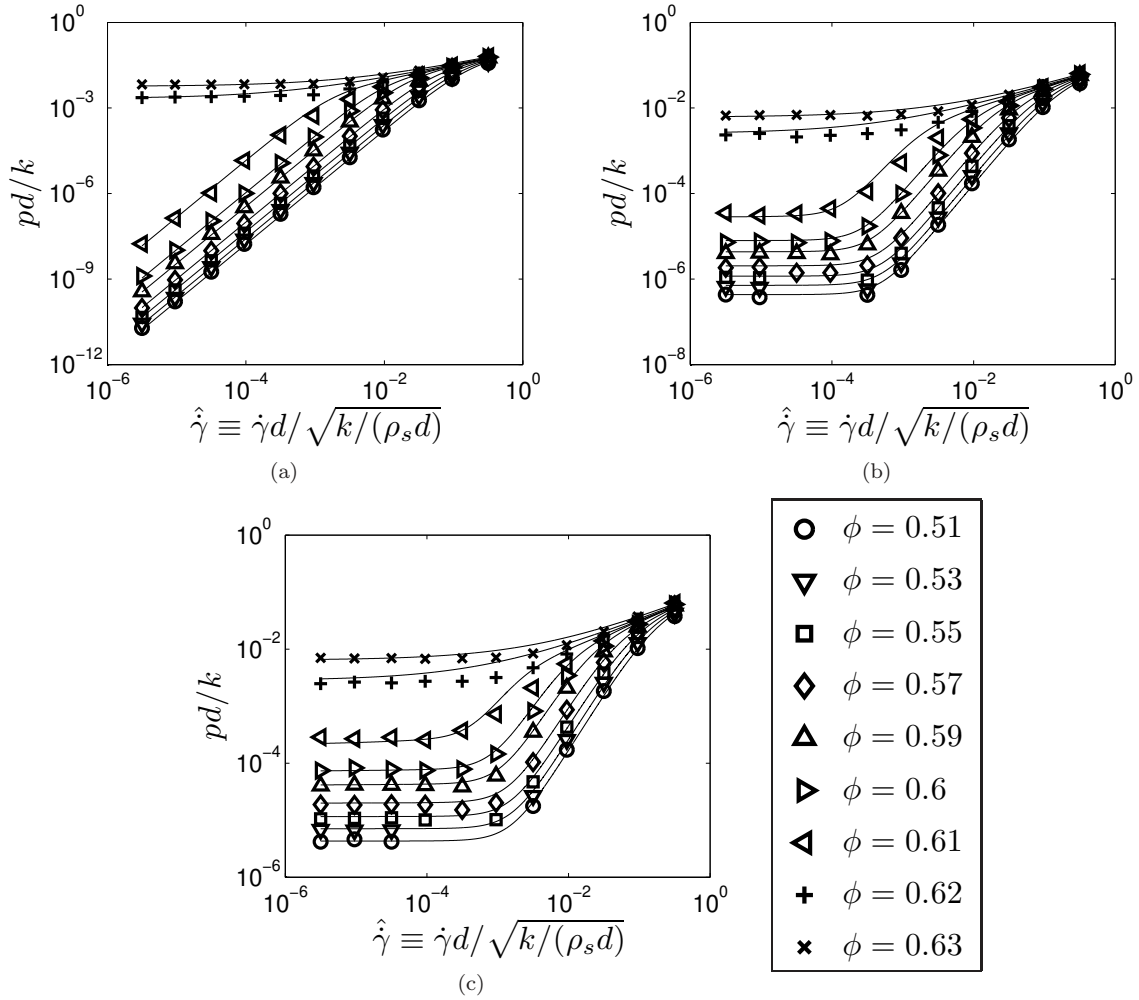
FIG. 1. Scaled pressure versus scaled shear rate for (a) non-cohesive particles, (b) cohesive particles with $Bo^* = 5 \times 10^{-6}$, (c) cohesive particles with $Bo^* = 5 \times 10^{-5}$. In all cases, Hookean contact and van der Waals force model are used, and interparticle friction coefficient $\mu = 0.1$. Symbols denote simulation results, while lines denote model predictions from Eqns. (10) - (12).

regime is obtained for non-cohesive systems, where both Z_{com} and Z_{ext} increase with shear rate (see Figure 5(b)). When the particles interact cohesively and the shear flow is in the cohesive regime, both Z_{com} and Z_{ext} are large at low shear rates (comparable in magnitude to those in the quasistatic regime) under low shear rate conditions. Increasing shear rate tends to break down the force chains in all quadrants, weakly at low shear rates and rapidly in the vicinity of $\sqrt{Bo^*}$, see Figure 5(b). Once a cohesive system enters the inertial regime, its behavior is similar to that of non-cohesive systems, with new contacts forming more readily leading to an increase in Z_{com} and Z_{ext}. It is the interplay between these two trends that give rise to a minimum in the average coordination number for cohesive systems in the vicinity of $\sqrt{Bo^*}$ (Figures 3(b) and 5(b)), and the regime transition observed in the pressure plot (Figure 4(b)).

IV. PRESSURE

A blended pressure model has been previously proposed for non-cohesive granular materials, which can capture the pressure continuously across different dense-flow regimes for different volume fractions and shear rates [2],

$$p = \begin{cases} p_{\mathrm{QS}} + p_{\mathrm{int}} & \text{for } \phi \geq \phi_c \\ (p_{\mathrm{inert}}^{-1} + p_{\mathrm{int}}^{-1})^{-1} & \text{for } \phi < \phi_c. \end{cases} \quad (6)$$

In this model, p_{QS}, p_{inert}, and p_{int} represent pressure in the quasistatic, inertial, and intermediate regimes. To model the transitions between them, a blending function B of the form $B(y_1, y_2) = (y_1^w + y_2^w)^{1/w}$ is used. $w = 1$ is chosen to create an additive blend for the quasistatic-to-intermediate transition and $w = -1$ is chosen to yield a harmonic blend for the inertial-to-intermedaite transition. Pressure in each individual regime is modeled based on scaling law similar to those in conventional critical
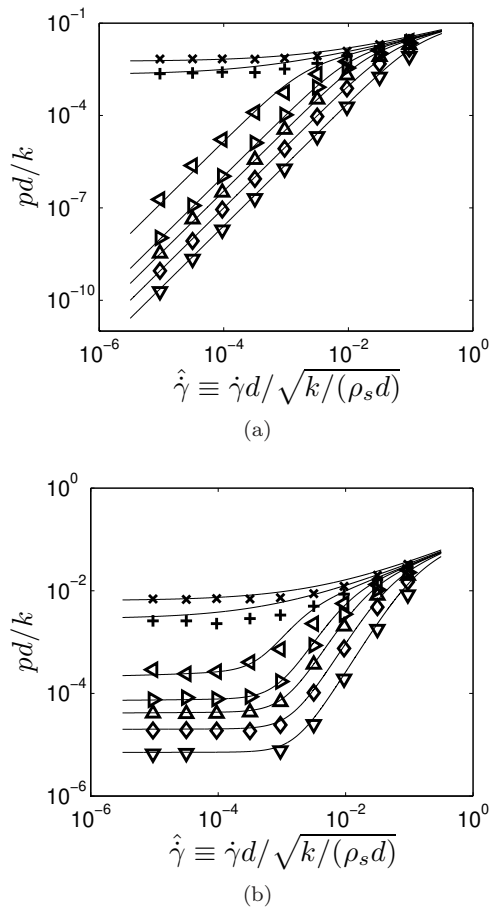
FIG. 2. Scaled pressure versus scaled shear rate for (a) non-cohesive particles, (b) cohesive particles with $Bo^* = 5 \times 10^{-5}$. Hookean contact and van der Waals force model are used, and interparticle friction coefficient $\mu = 0.1$ and restitution coefficient $e = 0.02$. Symbols denote simulation results at various volume fractions as per the legend from Figure 1. Lines denote model predictions from Eqn. (7) – (12). Model parameters used are the same as those in Table I.

TABLE I. Values of model constants

μ-dependent parameters			
μ	0.1	0.3	0.5
ϕ_c	0.614±0.001	0.596±0.001	0.587±0.001
χ	2.08±0.02	2.09 ±0.02	2.14±0.08
ϵ	1.00±0.01	0.92±0.01	0.67±0.02
α_{QS}	0.36	0.36	0.20
α_{int}	0.15	0.13	0.10
$\alpha_{coh,1}$	0.15	0.32	0.26
η_s	0.268	0.357	0.382
α_3	0.23	0.23	0.15

μ-independent parameters									
ϕ_a	α_{inert}	$\alpha_{coh,2}$	I_0	α_1	β_1	$\hat{\dot{\gamma}}_0$	α_2	β_2	α_4
0.45 ± 0.01	0.015	0.008	0.32	0.37	1.5	0.1	0.2	1.0	0.1

phenomena [36–39]. Specifically, one seeks a power-law relationship between pressure and shear rate in each flow regime [2]: $\frac{p_j}{|\phi - \phi_c|^\epsilon} \sim [\frac{\dot{\gamma}}{|\phi - \phi_c|^\omega}]^{m_j}$, $j = \text{QS, int, inert}$. In the rate-independent quasistatic regime, $m_{QS} = 0$. In the inertial regime, where pressure varies as the square of shear rate, $m_{inert} = 2$. Thus, assuming $p_{inert} \sim |\phi - \phi_c|^{-\chi}$, we set $\omega = (\epsilon + \chi)/2$. Furthermore, as the pressure is essentially independent of $|\phi - \phi_c|$ in the vicinity of the intermediate asymptote, we deduce that $m_{int} = \epsilon/\omega = 2\epsilon/(\epsilon + \chi)$. Thus, for non-cohesive particles with Hookean contact,

$$p_{QS} d/k = \alpha_{QS} |\phi - \phi_c|^\epsilon, \tag{7}$$

$$p_{int} d/k = \alpha_{int} \hat{\dot{\gamma}}^{2\epsilon/(\epsilon + \chi)}, \tag{8}$$

$$p_{inert} d/k = \frac{\alpha_{inert} \hat{\dot{\gamma}}^2}{|\phi_c - \phi|^\chi}. \tag{9}$$

The Levenberg-Marquardt method [40] is used to estimate the model constants. Details are included in Appendix B. As shown in Table I, it is found that α_{inert} is approximately independent of μ, while ϕ_c and α_{int} differ for different μ. The scaling exponent ϵ and prefactor α_{QS} in Eqn. (7), as well as the scaling exponent χ in Eqn. (9), manifest systematic dependence on μ, which was not reported by Chialvo et al. [2], who took $\chi = 2$ and $\epsilon = 2/3$ for all μ. Although it is not the principal focus of this study, we report in Table I the best-fit values of ϵ, α_{QS}, and χ for three different μ values. As demonstrated in Figures 6(a) and (b), Eqn. (7) and Eqn. (9) respectively capture the pressure in the quasistatic regime and inertial regime satisfactorily.

Furthermore, the resultant value of $m_{int} = 2\epsilon/(\epsilon + \chi)$ is consistent with experimental results [41, 42]. The effectiveness of the power-law relations is illustrated in Figure 7, where the pressure vs. shear rate data at several different volume fractions are collapsed on to two curves (one above ϕ_c and one below). Figures 7(a)-(c) show results for three different values of μ.

It has been noted previously in the literature [33] that the pressure in the quasistatic regime is not set by particle volume fraction (as in Eqn. (7)), and that it tracks more closely the average contact coordination number Z under both steady and dynamic flow conditions. In steady shear flows, Z is set by the particle volume fraction and so Eqn. (7) can be thought of the outcome of integrating a relation that applies under steady as well as dynamic conditions and one that is restricted to steady shear flows. Since stress is principally transmitted in the quasistatic regime through force chains, researchers have focused on Z_2, where particles with 0 or 1 contact are excluded as they are not involved in the force chains (e.g., see [33, 43]). We find that the pressure in the quasistatic regime can be expressed as $\alpha_Z (Z - Z_c(\mu))^2$ or $\alpha_{Z_2}(\mu)(Z_2 - Z_{2c}(\mu))^2$; see Figures 8(a) and (b). It is interesting to note that when the pressure is expressed in
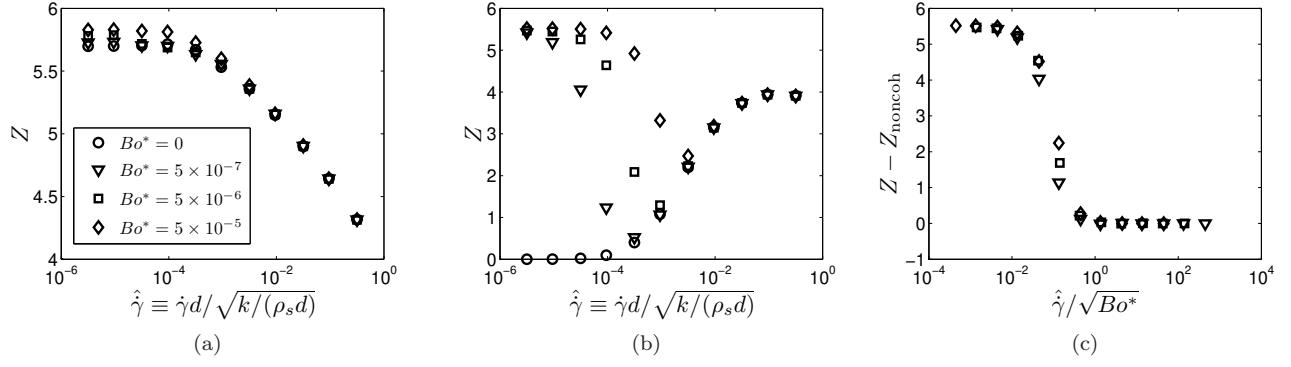
FIG. 3. The average coordination number versus scaled shear rate at $\mu = 0.1$ and various modified Bond numbers for (a) $\phi = 0.62$ and (b) $\phi = 0.59$. In (c), the data from (b) are collapsed into one curve by subtracting Z for non-cohesive system from that of cohesive systems and rescaling the shear rate. Hookean contact and van der Waals force model are used here.
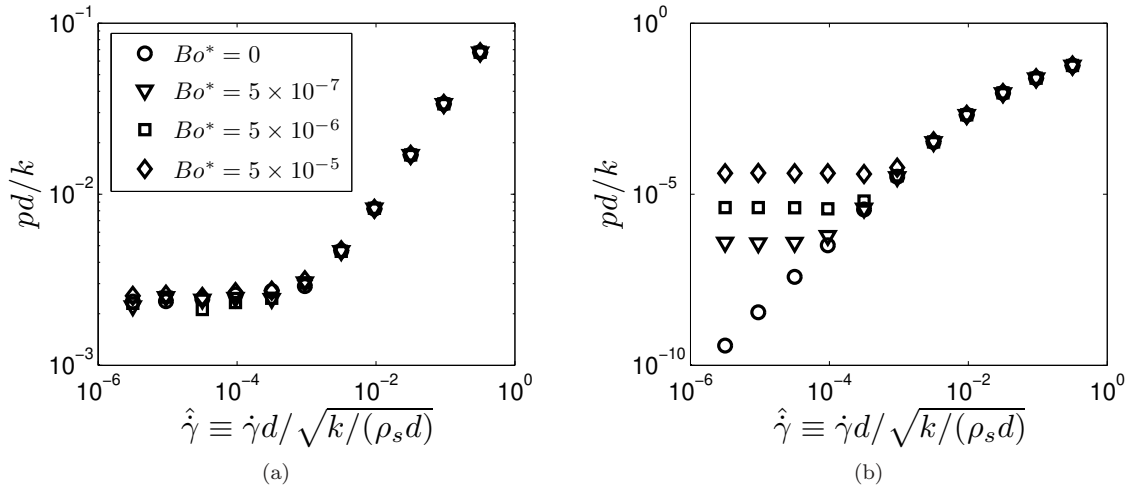

FIG. 4. Scaled pressure versus scaled shear rate at $\mu = 0.1$ and various modified Bond numbers for (a) $\phi = 0.62$ and (b) $\phi = 0.59$. Hookean contact and van der Waals force model are used here.
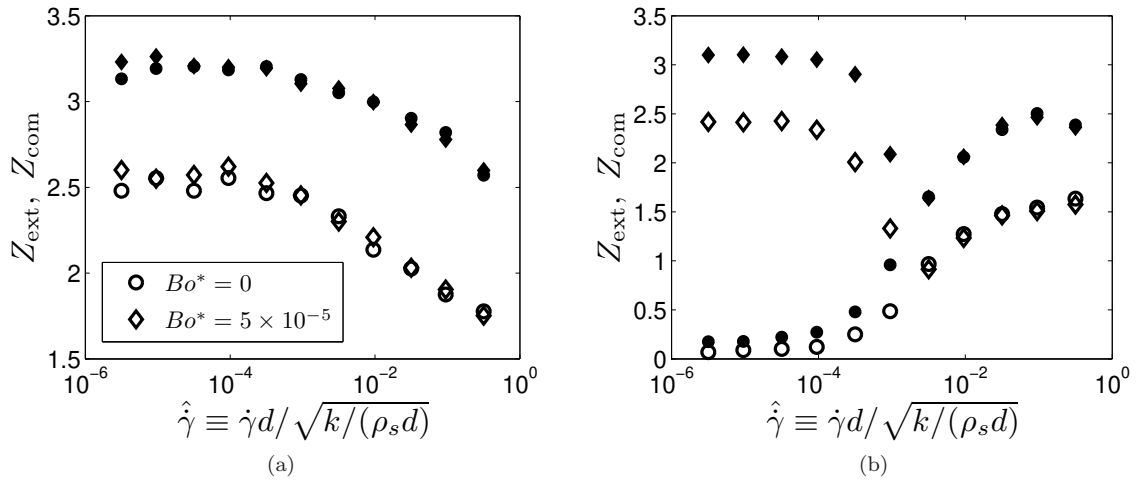
FIG. 5. The average coordination number in the extension quadrants (unfilled symbols) and compression quadrants (filled symbols) versus scaled shear rate at $\mu = 0.1$ for (a) $\phi = 0.62$ and (b) $\phi = 0.59$. Hookean contact and van der Waals force model are used here.
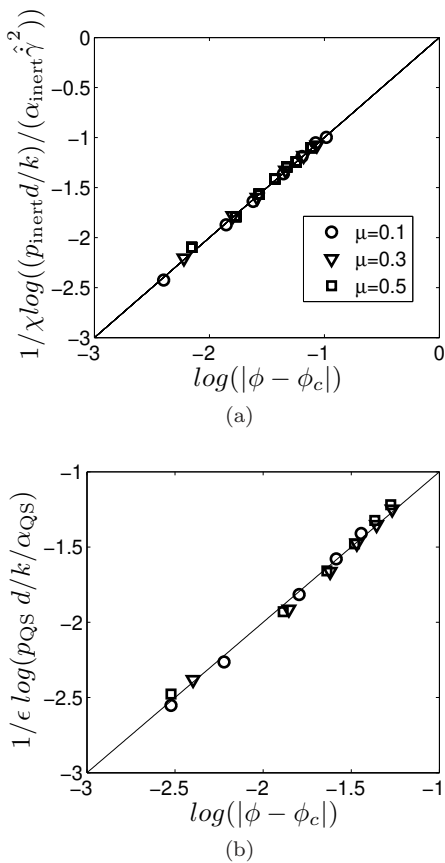
FIG. 6. Collapse of pressure for (a) inertial regime and (b) quasistatic regime. For both (a) and (b), the solid line has a slope of 1 and $y-$intercept of 0. All points with different volume fractions and particle friction coefficients fall on the lines. Hookean contact is used.

terms of Z or Z_2, the exponent is independent of μ; furthermore, when it is expressed in terms of Z (instead of Z_2), the proportionality constant is also independent of μ and the role of friction is manifested only through $Z_c(\mu)$. As seen in the caption for Figure 8(a) and (b), Z_c and Z_{2c} decrease as μ increases, which is consistent with previous results ([33, 34]). As seen in Figures 3(a) and 4(a), the pressure in the intermediate regime (and $\phi > \phi_c$) increases with shear rate, while Z decreases with increasing shear rate. This clearly shows that the relationship of the type shown in Figures 8(a) and (b) fail in the intermediate regime, even though the stress continues to be largely transmitted through force chains.

The pressure model for non-cohesive systems is readily modified to account for the effect of cohesion, as described below. The data reveal two trends which provide clues for constructing simple models. Firstly, as illustrated in Figure 10, $pd/k \sim Bo^*$ in the cohesive regime for all volume fractions (except for those near ϕ_c). This behavior is consistent with: (a) $pd/k \sim \hat{\dot{\gamma}}^2$ in the inertial regime and (b) the critical $\hat{\dot{\gamma}}$ value separating the inertial and cohesive regimes scales as $\sqrt{Bo^*}$. Figure 10 shows re-

sults down only to $\phi \approx 0.50$. At lower values of ϕ, the flow transitions to shear flows of agglomerates, and the size of the simulation domain used in this study is inadequate to get meaningful results. Secondly, while the intermediate asymptote (at $\phi = \phi_c$) given by Eqn. (8) persists for cohesive particles at high $\hat{\dot{\gamma}}$ values, it becomes rate-independent when $\hat{\dot{\gamma}}$ becomes small compared to a critical shear rate. This critical shear rate scales as $\sqrt{Bo^*}$, as shown in Figure 9; this is exactly the same dependence as observed earier for the cohesive-to-inertial transition. Together these observations suggest that, in the vicinity of ϕ_c, pd/k in cohesive regime scales as $(Bo^*)^{\epsilon/(\epsilon+\chi)}$.

Based on these observations, Eqn. (6) is adapted using the blending function previously described with $w = 1$ to provide an additive blend that can model both the cohesive-to-inertial and cohesive-to-intermediate transitions. Thus, the model becomes

$$
p = \begin{cases} p_{\mathrm{QS}} + (p_{\mathrm{int}} + p_{\mathrm{coh},2}) & \text{for } \phi \geq \phi_c \\ [(p_{\mathrm{inert}} + p_{\mathrm{coh},1})^{-1} + (p_{\mathrm{int}} + p_{\mathrm{coh},2})^{-1}]^{-1} & \text{for } \phi < \phi_c, \end{cases}
\tag{10}
$$

where p_{QS}, p_{int}, and p_{inert} are given by Eqns. (7)-(9), and

$$
p_{\mathrm{coh},1}d/k = \alpha_{\mathrm{coh},1}Bo^* \frac{|\phi - \phi_{\mathrm{a}}|}{|\phi_{\mathrm{c}} - \phi|},
\tag{11}
$$

$$
p_{\mathrm{coh},2}d/k = \alpha_{\mathrm{coh},2}(Bo^*)^{\epsilon/(\epsilon+\chi)}.
\tag{12}
$$

For non-cohesive particles, where $Bo^* = 0$, $p_{\mathrm{coh},1}$ and $p_{\mathrm{coh},2}$ vanish, and the proposed model returns to its original form written for non-cohesive particles. The Levenberg-Marquardt method [40] is again used to estimate the model constants. (Details are included in Appendix B.) They are provided in Table I. Predictions based on this pressure model are compared with the simulation results in Figure 1. The proposed model captures the data reasonably well not only in each regime but also in the transition regions.

V. SHEAR STRESS RATIO

Figure 11 displays the variation of stress ratio η (= τ/p) with the scaled shear rate $\hat{\dot{\gamma}}$ for both non-cohesive and cohesive particles with $\mu = 0.1$. Cohesion has a significant effect on the stress ratio only in the cohesive regime, where cohesion increases the stress ratio appreciably. This increase in stress ratio due to cohesion is in agreement with prior experiments [22] and simulations [18, 20, 23]. It is also consistent with increasing average coordination number with the inclusion of cohesion in the cohesive regime.

The stress ratio model for non-cohesive frictional granular materials proposed by Chialvo et al. [2] is composed of two contributions, η_{hard} and η_{soft}. The term η_{hard} is a function of inertial number $I \equiv \dot{\gamma}d/\sqrt{p/\rho_{\mathrm{s}}}$ and describes
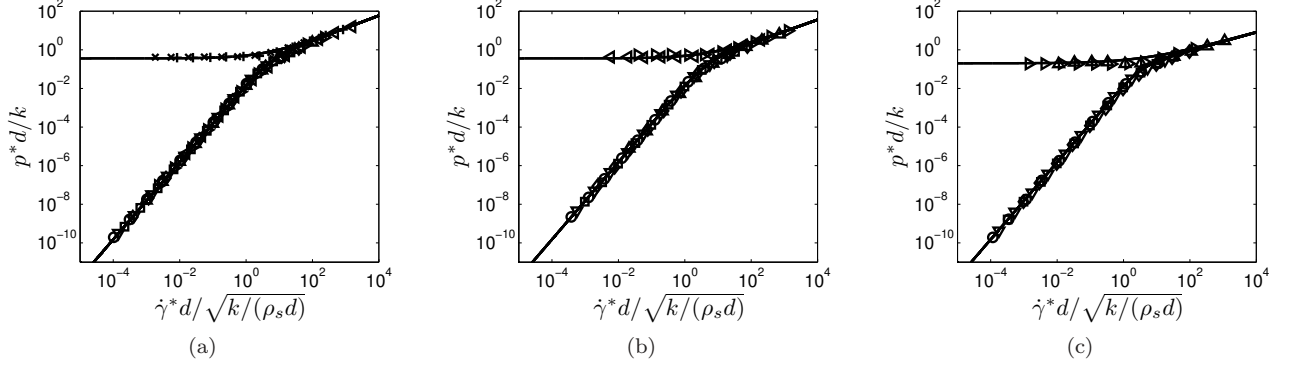
FIG. 7. Collapse of pressure versus shear rate curves for (a) $\mu = 0.1$, (b) $\mu = 0.3$, and (c) $\mu = 0.5$. In all cases, the pressure is scaled as $p^* = p/|\phi - \phi_c|^\epsilon$, and shear rate as $\dot{\gamma}^* = \dot{\gamma}/|\phi - \phi_c|^{(\epsilon+\chi)/2}$. (Values for ϵ and χ are included in Table I.) Symbols denote simulation results at various volume fractions as per the legend from Figure 1. The blending function, described in Eqns. (6)–(9) and represented by solid lines, captures regime asymptotes as well as transitions. Hookean contact with no cohesion is used.
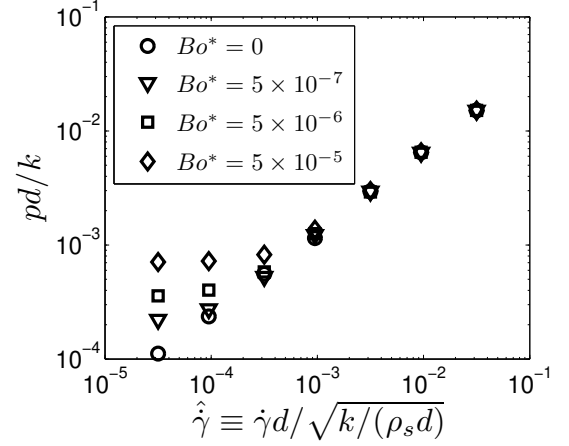

FIG. 9. Scaled pressure versus scaled shear rate at $\phi = 0.614$ for different cohesion levels (as shown in the legend). Inter-particle friction coefficient $\mu = 0.1$ is used. Hookean contact and van der Waals force model are used here.
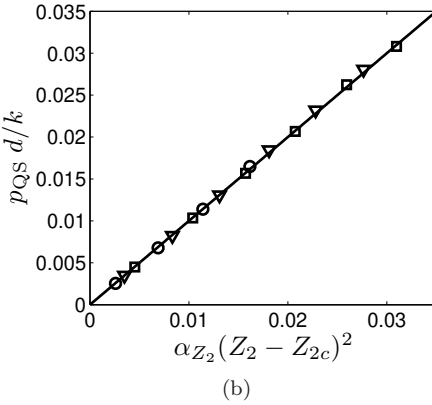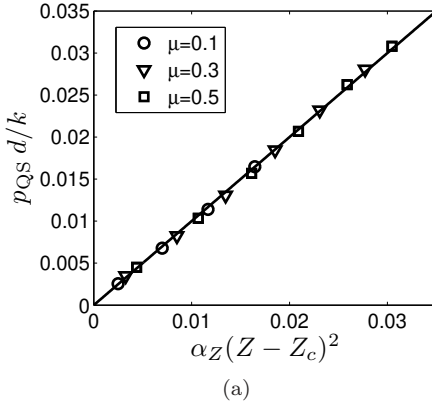
FIG. 8. Simulation data of scaled pressure in the quasistatic regime versus the predictions from the models based on (a) Z and (b) Z_2 for various volume fractions. In (a), $\alpha_Z = 0.007$, and $Z_c = 5.10$, 4.38, and 4.00 for $\mu = 0.1$, 0.3, and 0.5, respectively. In (b), $Z_{2c} = 5.20$, $\alpha_{Z_2} = 0.0077$ for $\mu = 0.1$; $Z_{2c} = 4.56$, $\alpha_{Z_2} = 0.0083$ for $\mu = 0.3$; and $Z_{2c} = 4.26$, $\alpha_{Z_2} = 0.0091$ for $\mu = 0.5$. The system is non-cohesive and Hookean contact is used. The line represents $y = x$.

the shear stress ratio for infinitely hard particles [8–10], while η_{soft} is a function of $\hat{\dot{\gamma}}$ and describes the deviation from hard-particle behavior due to finite stiffness:

$$\eta^* = \eta_{\text{hard}}(I) - \eta_{\text{soft}}(\hat{\dot{\gamma}}), \qquad (13)$$

$$\eta_{\text{hard}}(I) = \eta_{\text{s}}(\mu) + \frac{\alpha_1}{(I_0/I)^{\beta_1} + 1}, \qquad (14)$$

$$\eta_{\text{soft}}(\hat{\dot{\gamma}}) = \frac{\alpha_2}{(\hat{\dot{\gamma}}_0/\hat{\dot{\gamma}})^{\beta_2} + 1}. \qquad (15)$$

Here, η^* is the stress ratio for non-cohesive granular materials, and η_s is the yield stress ratio. The validity of this stress ratio model for non-cohesive granular materials is demonstrated in Figure 12. By correcting for particle
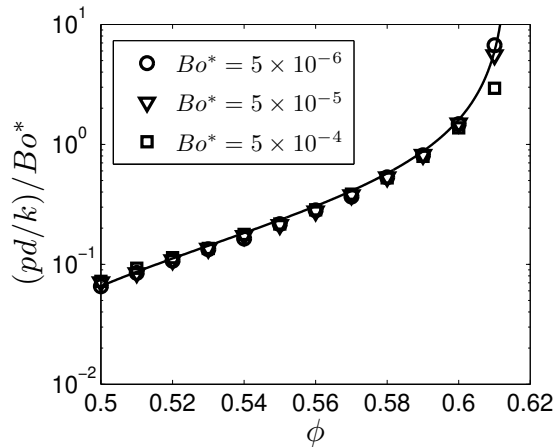
FIG. 10. Dimensionless pressure scaled by Bo^* versus volume fraction in the cohesive regime at $\hat{\gamma} = 3.2 \times 10^{-6}$ for $\mu = 0.1$ and various Bo^* values. The line represents $0.15 \frac{|\phi - \phi_a|}{|\phi_c - \phi|}$, where $\phi_c(\mu = 0.1) = 0.614$ and $\phi_a(\mu = 0.1) = 0.45$. Hookean contact and van der Waals force model are used here.

softness, the stress ratio data from all three regimes and particle friction coefficients are collapsed onto one curve.

As shown below, the well-known Mohr-Coulomb relation $\tau = \eta^* p + C$, which can be cast as

$$\eta = \eta^* + C/p, \tag{16}$$

captures our steady, simple shear flow simulation results in the rate-independent regimes, namely quasistatic and cohesive regimes, provided C is properly modeled. Rognon et al. [20] found that the model proposed by Rumpf [44] for C, $C_{\mathrm{Rumpf}} = Z\eta^*\phi Bo^* k/(\pi d)$, overestimates the value of C needed to match the simulation results. We found the same to be true as well. It is now known that Rumpf's formula does not account for non-affine particle displacements [45–48], which arise due to the structural disorder in the system. The relevance of nonaffine displacement has been investigated in the context of the shear modulus of covalent amorphous solids. He and Thorpe [49] performed simulations on randomly depleted covalent lattices, and found that, for the shear modulus G, $G = 0.33(Z - 2.4)^{1.42}$. Recent analytical theory by Zaccone [48] was applied to the same system and led to the expression, $G = 0.36(Z - 2.4)$. While this theory captured the critical coordination number well, there is a discrepancy between the theory and simulation results for the exponent and proportionality constant. In an analogous fashion, we accounted for the effect of non-affine displacement in our system by replacing Z in the Rumpf model with $a(Z - Z_n)^b$ so that

$$C_{\mathrm{Rumpf}}^{corr} = a(Z - Z_n)^b \eta^* \phi Bo^* k/(\pi d), \tag{17}$$

and sought if suitable choice of a, Z_n and b could capture our simulation results. We found that many combinations of these values yielded equally good fits, making

it difficult to discriminate among the different choices. For example, in the spirit of Zaccone [48], one could set $Z_n = 2.4$, $b = 1$ and allow a to be a function of μ and capture the data well (not shown). We found that we could get equally good fit by setting $a = b = 1$ and $Z_n = 3$ (where now all the parameters are independent of μ); this fit is illustrated in Figure 13. (As discussed later, $a = b = 1$ and $Z_n = 3$ captured the Hertzian contact results as well.) The simplicity of the fit with $Z_n = 3$ (as opposed to 2.4) could be due to the fact that microscopic models are different. For example, the cohesive force is active not only on the contacts that emerge due to cohesion, but also on those that form even in the absence of cohesion in our system, which differs from the system studied by He and Thorpe [49], and Zaccone [48]. In any case, our data do not permit more definitive analysis.

In the quasistatic and cohesive regimes, η^* is essentially η_s, and Z does not vary significantly with the shear rate (e.g., see Figures 3(a)(b)) and volume fraction (see results for the case of Hookean contact and van der Waals force model shown in Figure 14). In views of these, and since the coordination number is not directly accessible, a lumped model constant $\alpha_3 = (Z - Z_n)\eta_s/\pi$ is sufficient to capture our data:

$$\eta = \eta^* + \frac{\alpha_3 \phi Bo^* k/d}{p}. \tag{18}$$

To extend this model to cover rate-dependent regimes, namely inertial and intermediate, we modify the model as:

$$\eta = \eta^* + \frac{\alpha_3 \phi Bo^* k/d}{p} \frac{1}{\frac{\hat{\gamma}}{\alpha_4 \sqrt{Bo^*}} + 1}. \tag{19}$$

Here, $\alpha_4 \sqrt{Bo^*}$ approximates the critical shear rate which separates the cohesive and inertial regimes. When $\hat{\gamma} \ll \alpha_4 \sqrt{Bo^*}$, the model returns to Eqn. (18). When $\hat{\gamma} \gg \alpha_4 \sqrt{Bo^*}$, the second term in the model vanishes. The model describes stress ratio reasonably well for all Bo^* values considered without any changes to constitutive parameters, and for different μ values with slight adjustment of α_3. The values for α_3 and α_4 are listed in Table I.

VI. GENERALITY OF THE RESULTS

The newly identified regime map is preserved when the Hookean contact model is replaced by a Hertzian contact model as well as when the van der Waals force model is replaced with the alternate cohesion model of Rognon et al. [20]. The general form of the stress model is also preserved, albeit with small modifications. We illustrate these points by presenting two different particle-scale models: a) Hertzian contact and the van der Waals force model and b) Hookean contact and the alternative cohesion model (Eqn. (4)).
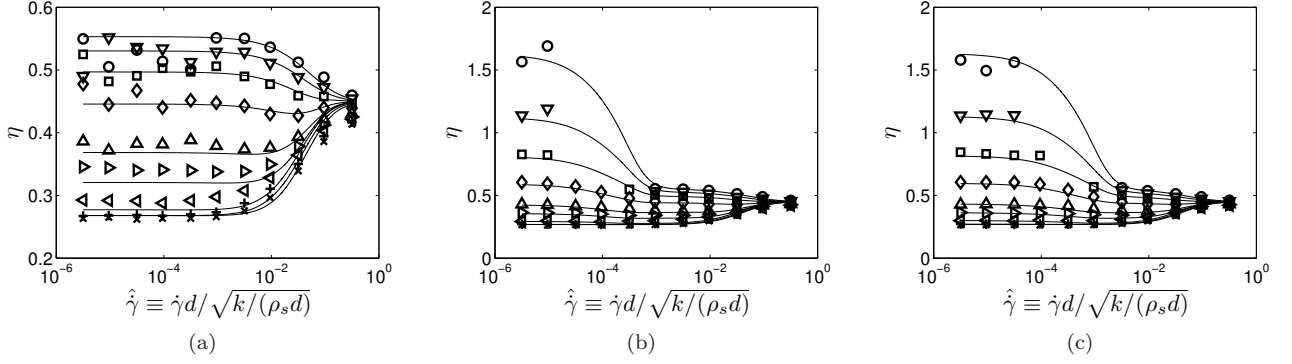
FIG. 11. Shear stress ratio versus scaled shear rate for (a) non-cohesive particles, (b) cohesive particles with $Bo^* = 5 \times 10^{-6}$, (c) cohesive particles with $Bo^* = 5 \times 10^{-5}$. In all cases, Hookean contact and van der Waals force model are used, and interparticle friction coefficient $\mu = 0.1$. Symbols denote simulation results at various volume fractions as per the legend from Figure 1. Lines denote model predictions from Eqns. (13) - (15) and (19).
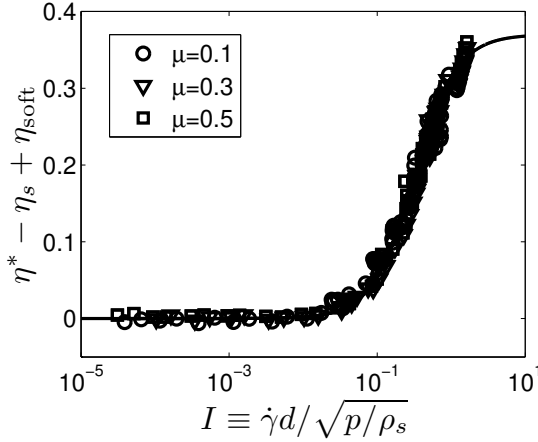

FIG. 12. The correction for particle softness yields a collapse of stress ratio data for non-cohesive particles in all three regimes for various particle friction coefficients (as shown in the legend). The line denotes the expression $\frac{\alpha_1}{(I_0/I)^{\beta_1}+1}$. Hookean contact is used.

FIG. 13. Predictions of $C_{\mathrm{Rumpf}}^{corr}/p$ taking account of non-affine displacements versus $\eta - \eta^*$ from simulation results for different volume fractions ($0.50 \leq \phi \leq \phi_c$), cohesion levels (as shown in the legend), and friction coefficients ($\mu = 0.1, 0.3,$ and 0.5) in the cohesive regime. In all cases, Hookean contact and van der Waals force model are used. The line represents $y = x$.

Flow Regimes

Figures 15(a) and (b) show the variation of scaled pressure against the scaled shear rate for cohesive particles from these two particle-scale models. The cohesive regime, characterized by rate-independent behavior below the critical volume fraction ($\phi_c = 0.614$ for $\mu = 0.1$ in the figures) and lower shear rates, is clearly present in both cases. In addition, simulation results from different Bo^* values confirm that the critical shear rate, separating the cohesive and inertial regimes, scales with $\sqrt{Bo^*}$ for both cases (not shown).
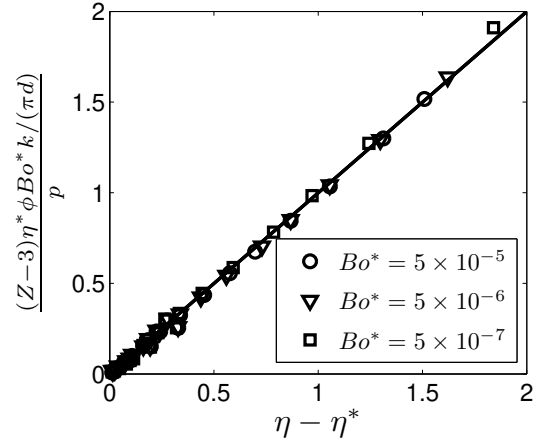
Pressure

The blended model for pressure, given by Eqn. (10), remains unaltered, but scalings for the various contributions there change when Hookean contact is replaced with Hertzian contact.

Specifically, $p_j d/k$ is changed to p_j/k. Therefore,

$$p_{\mathrm{QS}}/k = \alpha_{\mathrm{QS}}|\phi - \phi_{\mathrm{c}}|^\epsilon, \qquad (20)$$

$$p_{\mathrm{int}}/k = \alpha_{\mathrm{int}}\hat{\dot{\gamma}}^{2\epsilon/(\epsilon+\chi)}, \qquad (21)$$

$$p_{\mathrm{inert}}/k = \frac{\alpha_{\mathrm{inert}}\hat{\dot{\gamma}}^2}{|\phi_{\mathrm{c}} - \phi|^\chi}. \qquad (22)$$
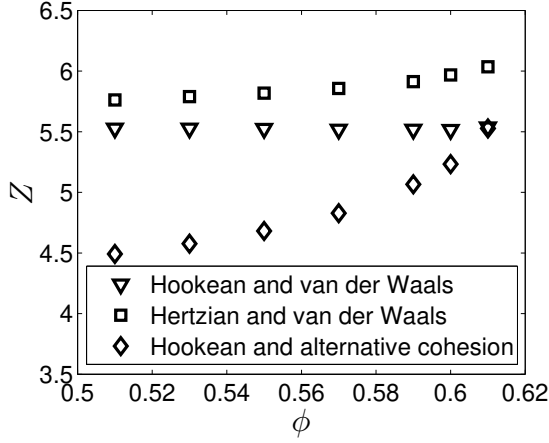
FIG. 14. The average coordination number versus volume fraction in the cohesive regime for particles with $\mu = 0.1$ and $Bo^* = 5 \times 10^{-5}$.

The Levenberg-Marquardt method [40] is performed to estimate the model constants. (Details can be referred to Appendix B.) It is found that $\chi = 1.43 \pm 0.03$. It is found that $\epsilon = 1.56$, 1.21, and 1.10 with uncertainties of ± 0.03 for $\mu = 0.1$, 0.3, and 0.5, respectively. The value of ϵ for Hertzian contact is approximately $3/2$ times the one for Hookean contact, which is consistent with previous results [33, 50]. Using the values for χ and ϵ, the pressure data can now be collapsed onto two curves for different μ, as illustrated in Figure 17 for the case of $\mu = 0.1$. Thus, Hertzian and Hookean contacts afford similar simulation results such that pressure can be collapsed in a similar fashion.

The first cohesive contribution $p_{\text{coh},1}$ remains unchanged from Eqn. (11) except for scaling on the left-hand side:

$$p_{\text{coh},1}/k = \alpha_{\text{coh},1} Bo^* \frac{|\phi - \phi_{\text{a}}|}{|\phi_{\text{c}} - \phi|}. \qquad (23)$$

Finally, since $p_{\text{coh},2}$ modifies the intermediate-regime contribution $(p_{\text{int}}/k \sim \hat{\dot{\gamma}}^{2\epsilon/(\epsilon+\chi)})$ and their sum becomes rate-independent for $\hat{\dot{\gamma}} \ll \sqrt{Bo^*}$, it is modified to scale as $Bo^{*\epsilon/(\epsilon+\chi)}$. This term now becomes

$$p_{\text{coh},2}/k = \alpha_{\text{coh},2}(Bo^*)^{\epsilon/(\epsilon+\chi)}. \qquad (24)$$

Model parameters used in the lines shown in Figure 15(a) are: $\chi = 1.43$, $\epsilon = 1.56$, $\alpha_{\text{QS}} = 0.19$, $\alpha_{\text{int}} = 0.15$, $\alpha_{\text{inert}} = 0.13$, $\alpha_{\text{coh},2} = 0.006$. Values for ϕ_c, ϕ_a, and $p_{\text{coh},1}$ are the same as those for Hookean contact with van der Waals force model (see Table I).

For case (b), the functional forms for the pressure model are unchanged, and Eqns. (7) – (12) are applied. Only values for ϕ_a, $\alpha_{\text{coh},1}$, and $\alpha_{\text{coh},2}$ are now different: $\phi_a = 0.50$, $\alpha_{\text{coh},1} = 1.2$, $\alpha_{\text{coh},2} = 0.03$.

Shear Stress Ratio

Stress ratio models are slightly modified for both cases and compared with the simulation data in Figures 16(a) and (b). For case (a), as noted earlier, $Z_n = 3$ captures our simulation results, and since Z does not change significantly with volume fraction (see results for the case of Hertzian contact and van der Waals force model shown in Figure 14), we can continue to lump $(Z - Z_n)\eta_s/\pi$ as α_3. As a result of change in the dimension of k for the Hertzian contact, Eqn. (19) now reads:

$$\eta = \eta^* + \frac{\alpha_3 \phi Bo^* k}{p} \frac{1}{\frac{\hat{\dot{\gamma}}}{\alpha_4 \sqrt{Bo^*}} + 1}, \qquad (25)$$

where η^* is described in Eqns. (13) – (15). Model parameters used in the lines shown in Figure 16(a) are: $\alpha_1 = 0.27$, $\alpha_2 = 0.23$, $\beta_1 = 1.0$, $\alpha_4 = 3$. Values for all the other parameters are the same as those for Hookean contact with the van der Waals force model.

For case (b), $Z_n = 0.5$ captures our simulation results adequately. Since Z changes significantly with volume fraction (see results for the case of Hookean contact and the alternative cohesion model shown in Figure 14), we find that modeling $(Z - Z_n)\eta_s/\pi$ as $\alpha_5(\phi - \phi_a)$ with $\alpha_5 = 10.3$ captures the stress ratio data well. As a result, Eqn. (19) is modified to the following:

$$\eta = \eta^* + \frac{\alpha_5(\phi - \phi_a)\phi Bo^* k/d}{p} \frac{1}{\frac{\hat{\dot{\gamma}}}{\alpha_4 \sqrt{Bo^*}} + 1}, \qquad (26)$$

where $\alpha_4 = 0.5$. The solid lines in Figure 16(b) correspond to Eqn. (26). Good agreement with simulation results is readily seen.

Note that different expressions for $(Z - Z_{\text{n}})\eta_s/\pi$ are needed to capture stress ratio results for van der Waals force model and alternative cohesion model. As noted earlier, the two cohesion models are significantly different: the van der Waals force saturates when the particles come to contact, while the cohesion is only present when the particles are in contact in the alternative cohesion model. Figure 14 illustrates the dependence of the coordination number on volume fraction for the three different cases presented in this article. For Hookean contact and van der Waals force model, Z is roughly independent from ϕ; for Hertzian contact and van der Waals force model, Z shows slight dependence on ϕ; and for Hookean contact and alternative cohesion model, Z increases appreciably with ϕ. This difference in response of coordination number to volume fraction helps explain the necessity of different expressions for $(Z - Z_{\text{n}})\eta_s/\pi$.

VII. SUMMARY

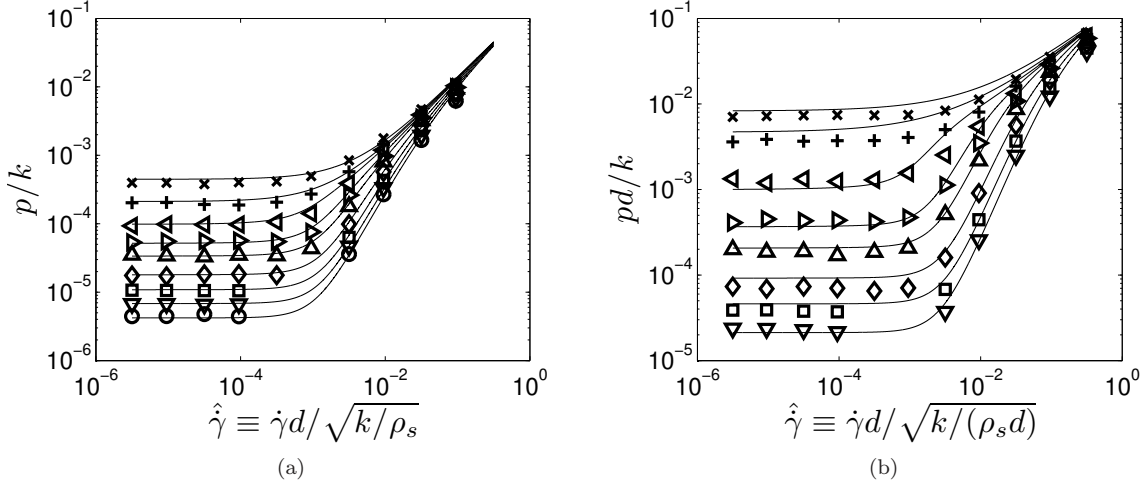We have investigated shear flows of dense cohesive granular materials via DEM simulations. The quasistatic

FIG. 15. Scaled pressure versus scaled shear rate for (a) Hertzian contact and the van der Waals force model, (b) Hookean contact and the alternative cohesion model [20]. Here, $\mu = 0.1$ and $Bo^* = 5 \times 10^{-5}$. Symbols denote simulation results at various volume fractions as per the legend from Figure 1. Lines denote model predictions from Eqns. (10) and (17) - (21) in (a), and Eqns. (10) - (12) in (b).
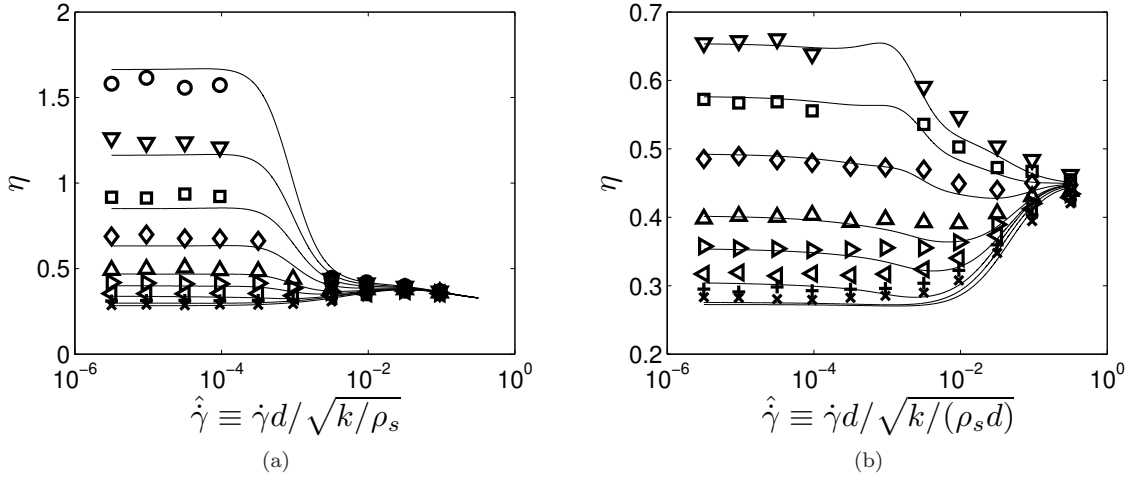

FIG. 16. Shear stress ratio versus scaled shear rate for (a) Hertzian contact and the van der Waals force model, (b) Hookean contact and the alternative cohesion model [20]. Here, $\mu = 0.1$ and $Bo^* = 5 \times 10^{-5}$. Symbols denote simulation results at various volume fractions as per the legend from Figure 1. Lines denote model predictions from Eqns. (13) - (15) and (25) in (a), and Eqns. (13) - (15) and (26) in (b).

and intermediate regimes observed for non-cohesive particles persist for cohesive particles, while the inertial regime of non-cohesive particles bifurcates into two regimes: rate-independent cohesive regime at low shear rates and inertial regime at higher shear rates. The regime map for the rheology of dense assemblies of cohesive particles is found to be robust even when the particle-scale details of the model are altered. Furthermore, the pressure and shear stress ratio results obtained in our simulations can be captured via simple algebraic expressions that can be used in conjunction with continuum models for flows in practical devices.

Appendix A: Inhomogeneously sheared state

In all the simple shear simulation results presented in the main text, the locally averaged velocity of the particles is verified to have a very nearly linear profile, and
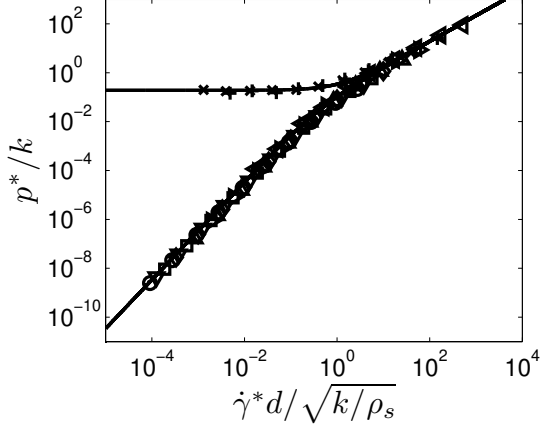
FIG. 17. Collapse of pressure versus shear rate curves for $\mu = 0.1$. The pressure is scaled as $p^* = p/|\phi - \phi_c|^\epsilon$, and shear rate as $\dot{\gamma}^* = \dot{\gamma}/|\phi - \phi_c|^{(\epsilon+\chi)/2}$. $\epsilon = 1.56$ and $\chi = 1.43$ is used. Symbols denote simulation results at various volume fractions as per the legend from Figure 1. The blending function, described in Eqns. (20)–(22) and represented by solid lines, captures regime asymptotes as well as transitions. Hertzian contact with no cohesion is used.
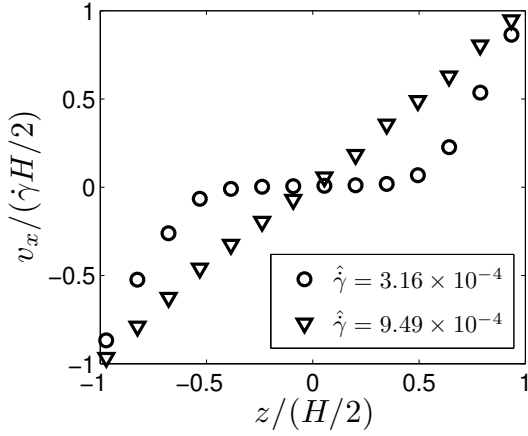

FIG. 18. Locally averaged velocity versus position in the direction of shear. Domain-averaged volume fraction of particles is 0.51. Hookean contact and van der Waals force model are used with $\mu = 0.1$ and $Bo^* = 5 \times 10^{-6}$. H denotes the thickness of the periodic box in the shear direction.

the particle volume fraction profile is uniform. For cohesive particles, shear flow simulations yield inhomogeneous volume fraction and velocity fields at the lower volume fractions considered in this study (namely, $\phi \approx 0.5$) and at shear rates in the vicinity of the transition between cohesive and inertial regimes. Figure 18 shows the scaled velocity profiles for two different scaled shear rates and domain-averaged volume fraction of 0.51. All other conditions are as in Figure 1(b). It is readily seen that a linear velocity profile was achieved for $\hat{\dot{\gamma}} = 9.49 \times 10^{-4}$ (results included in Figure 1(b)), but not for $\hat{\dot{\gamma}} = 3.16 \times 10^{-4}$

(and hence omitted from Figure 1(b)). It appears reasonable to hypothesize that the occurrence of an inhomogeneous state is a manifestation of shear-banding instability [51, 52] which has not been a focus of the present study but merits future investigation.

Appendix B: Model constants determination

The Levenberg-Marquardt method [40] is used to estimate the critical exponents as well as the values for ϕ_c and ϕ_a in the pressure models for the inertial, quasistatic and cohesive regimes. Here, we use the case of Hookean contact and the van der Waals force model to detail the process of using this method to arrive at the values as shown in Table I.

For the pressure model in the inertial regime, the functional form $\frac{p_{\text{inert}} d/k}{\hat{\dot{\gamma}}^2} = \frac{\alpha_{\text{inert}}}{|\phi_c - \phi|^\chi}$ is assumed. The Levenberg-Marquardt method is used to estimate ϕ_c and χ from simulation results for non-cohesive particles at various shear rates with ϕ as the independent variable and $\frac{p_{\text{inert}} d/k}{\hat{\dot{\gamma}}^2}$ as the dependent variable. The values of χ and ϕ_c for different particle friction coefficients are found and included in Table I.

For the pressure in the quasistatic regime, the functional form $p_{\text{QS}} d/k = \alpha_{\text{QS}} |\phi - \phi_c|^\epsilon$ is assumed. The Levenberg-Marquardt method is performed to estimate ϕ_c and ϵ from simulation results for non-cohesive particles at various shear rates with ϕ as the independent variable and $p_{\text{QS}} d/k$ as the dependent variable. The values for ϕ_c are found to be close to the ones previously determined in the inertial regime. These previously determined ϕ_c values are then used to estimate ϵ, which are reported in Table I.

For the pressure in the cohesive regime, the functional form $\frac{p_{\text{coh},1} d/k}{Bo^*} = \alpha_{\text{coh},1} \frac{|\phi - \phi_a|}{|\phi_c - \phi|}$ is assumed. The Levenberg-Marquardt method is again performed to estimate ϕ_a and ϕ_c from simulation results for cohesive particles at various shear rates and modified Bond values with ϕ as the independent variable and $\frac{p_{\text{coh},1} d/k}{Bo^*}$ as the dependent variable. The values for ϕ_c are found to be close to the ones previously determined in the inertial regime. These previously determined ϕ_c values are then used to estimate ϕ_a. It is found that ϕ_a is 0.45 ± 0.01, 0.45 ± 0.01, and 0.44 ± 0.01 for $\mu = 0.1$, 0.3, and 0.5, respectively. Thus, the values for ϕ_a are the same for different particle friction coefficients within uncertainties. In Table I of the manuscript, we only report one value for ϕ_a for different particle friction coefficients.

[1] C. S. Campbell, J. Fluid Mech. **465**, 261 (2002).
[2] S. Chialvo, J. Sun, and S. Sundaresan, Phys. Rev. E **85**, 021305 (2012).
[3] M. Otsuki and H. Hayakawa, Phys. Rev. E **83**, 051301 (2011).
[4] G. Lois and J. M. Carlson, Eur. Lett. **80**, 58001 (2007).
[5] T. Hatano, J. Phys. Soc. Jpn. **77**, 123002 (2008).
[6] M. Otsuki and H. Hayakawa, Phys. Rev. E **80**, 011308 (2009).
[7] K. N. Nordstrom, E. Verneuil, P. E. Arratia, A. Basu, Z. Zhang, A. G. Yodh, J. P. Gollub, and D. J. Durian, Phys. Rev. Lett. **105**, 175701 (2010).
[8] F. da Cruz, S. Emam, M. Prochnow, J.-N. Roux, and F. Chevoir, Phys. Rev. E **72**, 021309 (2005).
[9] G. D. R. MiDi, Eur. Phys. J. E **14**, 341 (2004).
[10] P. Jop, Y. Forterre, and O. Pouliquen, Nature **441**, 727 (2006).
[11] A. Castellanos, Adv. Phys. **54**, 263 (2005).
[12] M. A. S. Quintanilla, A. Castellanos, and J. M. Valverde, Phys. Rev. E **64**, 031301 (2001).
[13] M. F. Al-Adel, D. A. Saville, and S. Sundaresan, Ind. Eng. Chem. Res. **41**, 6224 (2002).
[14] A. Forsyth, S. Hutton, and M. Rhodes, Powder Technol. **126**, 150 (2002).
[15] K. Kuwagi, T. Mikami, and M. Horio, Powder Technol. **109**, 27 (2000).
[16] B. Ennis, Powder Technol. **65**, 257 (1991).
[17] M. Weber, D. Hoffman, and C. Hrenya, Granul. Matter **6**, 239 (2004).
[18] L. Aarons and S. Sundaresan, Powder Tech. **169**, 10 (2006).
[19] R. Mei, H. Shang, O. R. Walton, and J. F. Klausner, Powder Technol. **112**, 102 (2000).
[20] P. G. Rognon, J.-N. Roux, M. Naaïm, and F. Chevoir, J. Fluid Mech. **596**, 21 (2008).
[21] R. Brewster, G. S. Grest, J. W. Landry, and A. J. Levine, Phys. Rev. E **72**, 061301 (2005).
[22] J. F. Klausner, D. Chen, and R. Mei, Powder Technol. **112**, 94 (2000).
[23] I. Iordanoff, N. Fillot, and Y. Berthier, Powder Technol. **159**, 46 (2005).
[24] S. Nase, W. Vargas, A. Abatan, and J. McCarthy, Powder Technol. **116**, 214 (2001).
[25] P. Tegzes, T. Vicsek, and P. Schiffer, Phys. Rev. Lett. **89**, 094301 (2002).
[26] P. Tegzes, T. Vicsek, and P. Schiffer, Phys. Rev. E **67**, 051303 (2003).
[27] A. W. Alexander, B. Chaudhuri, A. Faqih, F. J. Muzzio, C. Davies, and M. S. Tomassone, Powder Technol. **164**, 13 (2006).
[28] P. A. Cundall and O. D. L. Strack, Géotechnique **29**, 47 (1979).
[29] R. Y. Yang, R. P. Zou, and A. B. Yu, Phys. Rev. E **62**, 3900 (2000).
[30] S. Plimpton, J. Comput. Phys. **117**, 1 (1995).
[31] J. Shäfer, S. Dippel, and D. E. Wolf, J. Phys. I **6**, 5 (1996).
[32] A. W. Lees and S. F. Edwards, J. Phys. C **5**, 1921 (1972).
[33] J. Sun and S. Sundaresan, J. Fluid Mech. **682**, 590 (2011).
[34] C. Song, P. Wang, and H. A. Makse, Nature **453**, 629 (2008).
[35] C. S. Campbell and C. E. Brennen, J. Fluid Mech. **151**, 167 (1985).
[36] C. S. O'Hern, S. A. Langer, A. J. Liu, and S. R. Nagel, Phys. Rev. Lett. **88**, 075507 (2002).
[37] C. S. O'Hern, L. E. Silbert, A. J. Liu, and S. R. Nagel, Phys. Rev. E **68**, 011306 (2003).
[38] P. Olsson and S. Teitel, Phys. Rev. Lett. **99**, 178001 (2007).
[39] M. Otsuki and H. Hayakawa, Prog. Theor. Phys. **121**, 647 (2009).
[40] P. Olsson and S. Teitel, Phys. Rev. E **83**, 030302 (2011).
[41] J. R. Seth, M. Cloitre, and R. T. Bonnecaze, J. Rheol. **52**, 1241 (2008).
[42] J. R. Seth, L. Mohan, C. Locatelli-Champagne, M. Cloitre, and R. T. Bonnecaze, Nat. Mater. **10**, 838 (2011).
[43] K. Shundyak, M. van Hecke, and W. van Saarloos, Phys. Rev. E **75**, 010301 (2007).
[44] H. Rumpf, Chemie Ing. Tech. **30**, 144 (1958).
[45] A. Zaccone and E. Scossa-Romano, Phys. Rev. B **83**, 184205 (2011).
[46] A. Zaccone and E. M. Terentjev, Phys. Rev. Lett. **110**, 178002 (2013).
[47] A. Zaccone and E. M. Terentjev, J. Appl. Phys. **115**, 033510 (2014).
[48] A. Zaccone, Mod. Phys. Lett. B **27**, 1330002 (2013).
[49] H. He and M. F. Thorpe, Phys. Rev. Lett. **54**, 2107 (1985).
[50] H. P. Zhang and H. A. Makse, Phys. Rev. E **72**, 011301 (2005).
[51] B. Utter and R. P. Behringer, Phys. Rev. E **69**, 031308 (2004).
[52] A. Singh, V. Magnanimo, K. Saitoh, and S. Luding, Phys. Rev. E **90**, 022202 (2014).